Check for updates

Tuning Cation (Dis)Order in Cr-Based Li-Excess Oxide Cathode Materials to Improve Li$^+$ Transport Properties

*Maciej Moździerz, Tucker Holstun, Zijian Cai, Gi-Hyeok Lee, Han-Ming Hau, Xiaochen Yang, Yu Chen, Paweł Czaja, Wanli Yang, Konrad Świerczek, and Gerbrand Ceder**

Li-excess disordered rocksalts (DRXs) hold promise as next-generation cathodes for Li-ion batteries due to their high capacity and energy density, along with the potential to eliminate the need for Co and Ni. However, due to their low Li$^+$ diffusivity, DRXs need to be pulverized into nanoparticles to achieve high performance. Herein, a new strategy for overcoming this limitation is demonstrated, involving the design of as-synthesized partially disordered oxides with a structure that lies between ordered layered and fully disordered, exhibiting a varying degree of local (dis)order. This unique structure activates new Li$^+$ diffusion channels, improving percolation and transport properties. This strategy allows a large content of Li$^+$ to be accessed in material with large, micron-sized particles through highly reversible Cr$^{3+/6+}$ and O redox, yielding a first discharge capacity of 286 mAh g^{-1} (881 Wh kg^{-1}). The Li$^+$ percolation network is further improved by substituting Ti with a mixture of multiple metals, which appears to locally decrease the migration barrier through lattice distortion. Proper tuning of the chemical composition, especially the content of metals with empty *d* orbitals, is established as a crucial factor for controlling the degree of disorder and mitigating voltage fade and hysteresis growth upon cycling.

1. Introduction

The ongoing growth of the Li-ion battery market, along with its expansion into electric vehicles and large-scale grid storage, has created a demand for higher energy and power density in batteries, as well as a reduction in their cost.[1,2] This can be achieved by replacing the currently widely used layered cathode materials containing Co and Ni, such as $Li(Ni_{1-x-y}Mn_xCo_y)O_2$ and $Li(Ni_{1-x-y}Co_xAl_y)O_2$, with other high-energy-density materials that rely on earth-abundant elements.[1,3–5] One of the most promising groups of future cathodes, consisting entirely of earth-abundant metals such as Mn, Ti, and Cr, are disordered rocksalts with Li-excess (DRXs). These materials can provide energy densities of up to 1000 Wh kg^{-1} and specific capacities reaching 300 mAh g^{-1}.[6–9] Their recent development was enabled by theoretical insights into Li$^+$ diffusion in oxides with face-centered cubic (FCC) oxygen framework.[7,10] Li$^+$ jumps between two octahedral sites primarily occur through intermediate tetrahedral sites (o-t-o diffusion).[10] The barrier for o-t-o diffusion is governed by the tetrahedron height and the type of cations face-sharing with the tetrahedron. As such, any tetrahedron can be categorized as an active or

---

M. Moździerz, T. Holstun, Z. Cai, H.-M. Hau, X. Yang, Y. Chen, G. Ceder
Lawrence Berkeley National Laboratory
Materials Sciences Division
Berkeley, CA 94720, USA
E-mail: gceder@berkeley.edu

M. Moździerz, K. Świerczek
Faculty of Energy and Fuels
AGH University of Krakow
al. Mickiewicza 30, Krakow 30-059, Poland

The ORCID identification number(s) for the author(s) of this article can be found under https://doi.org/10.1002/aenm.202502157

© 2025 The Author(s). Advanced Energy Materials published by Wiley-VCH GmbH. This is an open access article under the terms of the Creative Commons Attribution-NonCommercial-NoDerivs License, which permits use and distribution in any medium, provided the original work is properly cited, the use is non-commercial and no modifications or adaptations are made.

DOI: 10.1002/aenm.202502157

T. Holstun, Z. Cai, H.-M. Hau, X. Yang, Y. Chen, G. Ceder
Department of Materials Science and Engineering
University of California Berkeley
Berkeley, CA 94720, USA

G.-H. Lee, W. Yang
Lawrence Berkeley National Laboratory
Advanced Light Source
Berkeley, CA 94720, USA

P. Czaja
Institute of Metallurgy and Materials Science
Polish Academy of Sciences
ul. Reymonta 25, Krakow 30-059, Poland

K. Świerczek
AGH Centre of Energy
AGH University of Krakow
ul. Czarnowiejska 36, Krakow 30-054, Poland

16146840, 0, Downloaded from https://advanced.onlinelibrary.wiley.com/doi/10.1002/aenm.202502157, Wiley Online Library on [16/06/2025]. See the Terms and Conditions (https://onlinelibrary.wiley.com/terms-and-conditions) on Wiley Online Library for rules of use; OA articles are governed by the applicable Creative Commons License

inactive diffusion channel by the number of transition metals (TMs) which face-share with it.[10] In Li-stoichiometric ordered layered oxides, only 1-TM channels are available for Li^+ hops, and the migration barrier for these channels increases with cation mixing.[7,10] However, if the degree of disorder is high enough and there is sufficient Li-excess, 0-TM channels, tetrahedral sites which do not face-share with a TM, can form a percolating network and enable macroscopic Li^+ diffusion.[7,10] While the 0-TM network is the main diffusion pathway in DRXs, 1-TM channels may also be active to some degree.[11–13] Nevertheless, the Li^+ diffusivity in DRX materials (10^{-16}–10^{-15} cm^2 s^{-1}) is lower than in conventional layered cathodes (10^{-10}–10^{-9} cm^2 s^{-1}).[14,15] To achieve good electrochemical performance, DRX particles need to be pulverized to shorten the diffusion length, either through ball-milling after a solid-state synthesis or by using a mechanochemical (ball-milling) synthesis method.[9,14–20] Eliminating this milling step is one of the challenges for the future commercialization of DRX-based materials.[14,16,17,21] Several strategies have been proposed to improve Li^+ transport kinetics. Introducing cations capable of reversibly migrating from octahedral to tetrahedral sites, such as $Cr^{3+/6+}$,[22] $V^{3+/5+}$,[23] and $Mo^{3+/6+}$,[24] has been demonstrated to enhance the percolation network by increasing the amount and connectivity of 0-TM channels.[22] DRX materials also typically exhibit significant deviations from a random cation distribution due to short-range order (SRO), which may worsen 0-TM percolation.[25,26] Unfavorable SRO can be efficiently suppressed by using a high-entropy approach, which creates a more random configuration of cations, leading to a significant improvement in energy density and rate capability.[27–29] SRO can also be controlled by optimizing synthesis conditions,[30] introducing layered-like ordering,[26,31] or using partial Li deficiency.[19] Additionally, a partial transformation of DRX into a spinel-like δ phase can substantially improve transport properties, leading to better energy density and rate capability.[21,32,33] Despite improvements to the apparent diffusivity of the DRX in most previous reports, ball-milling was utilized before electrode preparation.

Interestingly, previous calculations[7,10] indicate that 0-TM percolation is more readily achieved in a partially cation-mixed layered structure than in a fully disordered one, making it an intriguing possible route to partially (dis)ordered structures with good rate capability and high energy content. In this work, we aim to achieve a partially disordered (PD) structure in as-synthesized materials, specifically in Li-excess systems based on $Cr^{3+/6+}$ redox: $Li_{1.2}Cr_{0.4}Ti_{0.4}O_2$ (LCT) and $Li_{1.2}Cr_{0.4}Ti_{0.2}Al_{0.05}Mn_{0.05}Fe_{0.05}Mo_{0.05}O_2$ (LCT-HE). While LCT has been previously studied as a potential cathode material, showing a high capacity of ca. 200 mAh g^{-1} (2.0–4.8 V),[34–37] the Li^+ diffusion pathways, detailed structural properties, origins of voltage hysteresis, and redox mechanism have not been fully elucidated. Here, we thoroughly study the PD structure, demonstrating that it can be considered an intermediate between a fully disordered rocksalt phase and an ordered layered phase. This structure is characterized by the average cation mixing parameter but exhibits a locally varying, inhomogeneous degree of (dis)order. We use these findings to explain why the PD oxides exhibit enhanced Li^+ transport properties, outperforming conventional DRX cathodes. We introduce the content of elements with empty *d* orbitals (d^0 configuration) as a key parameter for designing these materials. We address the issues with hysteresis growth in LCT by proposing a new composition, LCT-HE, which delivers stable and non-hysteretic performance with a high energy density of 881 Wh kg^{-1} within a 1.5–4.8 V voltage window. The overall improved Li^+ kinetics, combined with the relatively low synthesis temperature, enables the developed materials to work effectively in their as-synthesized form, constituting a new and promising pathway toward novel cathode materials.

2. Results

2.1. Design and Characterization of the Partially Disordered Layered Structure

In a layered O3 structure, discrete Li layers and transition metal (TM) layers are stacked alternately along the c-axis.[38,39] When Li-excess is introduced, some of the metals in the TM layer are replaced by Li^+, often forming honeycomb ordering.[38,39] In a fully disordered rocksalt, 50% of TMs are located in each hypothetical layer. The partially disordered (PD) structure can be considered as an intermediate between these two structures. It can be characterized by the percentage of cation mixing, defined as TM occupancy in the Li layer divided by TM occupancy in the TM layer (cation mixing = 0% for ordered layered; cation mixing = 100% for fully disordered oxide). Our goal here is to explore the electrochemical properties of PD oxides, designed by carefully adjusting their chemical composition. In general, a high ionic radii mismatch between Li^+ and a given cation in octahedral coordination favors independent relaxation of Li-O and metal-O bonds, promoting the formation of the layered structure.[6,40] On the other hand, a disordered local environment can be stabilized by d^0 cations, as they allow for accommodating large distortions of the octahedra.[6,40,41] Based on these rules, Li-excess $Li_{1.2}Cr_{0.4}Ti_{0.4}O_2$ (LCT) appears to be a good candidate for obtaining the desired PD structure, as it has an equimolar ratio between Cr^{3+} (which exhibits a high tendency to form the layered phase[27,29]) and d^0 Ti^{4+}. Also, incorporating Cr^{3+} is of high interest since it can undergo three-electron redox upon oxidation to Cr^{6+}, potentially providing a very high capacity without significant contribution from O redox, which, when used to a large extent, may be irreversible and lead to O_2 release.[42] Another proposed composition, which should allow for obtaining the PD structure, is $Li_{1.2}Cr_{0.4}Ti_{0.2}Al_{0.05}Mn_{0.05}Fe_{0.05}Mo_{0.05}O_2$. We refer to this multicomponent-doped material as LCT-HE because it shares a common Cr content with LCT but has 0.2 mol of Ti substituted by a mixture of four cations in an equimolar ratio, making it a high-entropy oxide (HEO, Table S1 and Note S1, Supporting Information).[43] Also, we plan to investigate possible synergistic effects stemming from the presence of multiple different cations in the structure, which should influence electrochemical performance, as has been reported for other HEOs.[27,44] Assuming the targeted oxidation states of the cations (Al^{3+}, Mn^{4+}, Fe^{3+}, Mo^{6+}), LCT-HE should be more layered-like (with less interlayer mixing) than LCT due to the presence of Mn^{4+} and Al^{3+} (replacing Ti^{4+}), which are commonly incorporated into cathode materials to stabilize the layered structure.[45–49] Meanwhile, Fe^{3+} and Mo^{6+} are expected to possess a similar tendency toward disorder as Ti^{4+}.

Both LCT and LCT-HE were synthesized by a solid-state synthesis method at 850 °C. The X-ray diffraction (XRD) patterns in

© 2025 The Author(s). Advanced Energy Materials published by Wiley-VCH GmbH

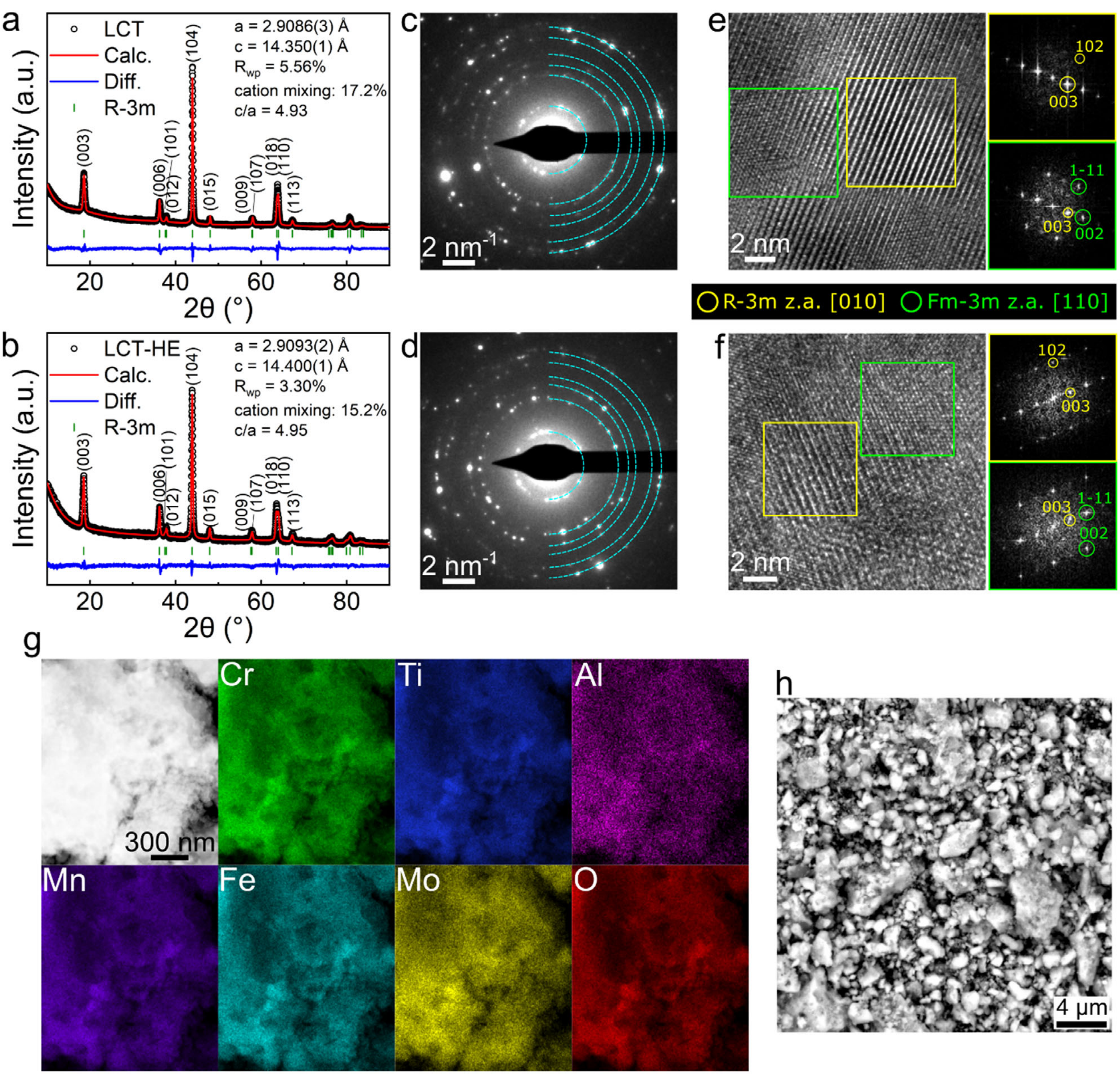

Figure 1. Structural characterization of the PD layered oxides. a,b) XRD patterns with Rietveld refinement for R-3m layered structure (single-phase model with cation mixing) for (a) LCT and (b) LCT-HE with the extracted structural parameters. c,d) SAED patterns for (c) LCT and (d) LCT-HE with the rings assigned to the layered R-3m structure. The measured d-spacings are equal to 4.74, 2.43, 2.02, 1.86, 1.58, 1.43 Å for LCT (c) and 4.66, 2.34, 2.04, 1.85, 1.57, 1.44 Å for LCT-HE (d). e,f) HR-TEM images for (e) LCT and (f) LCT-HE with the corresponding FFT highlighting layered-like (yellow color, R-3m, zone axis [010]) and partially-mixed (rocksalt-like features, green color, Fm-3m, zone axis [110]) regions. g) STEM image with the corresponding EDS maps for LCT-HE. h) SEM image for LCT-HE.

Figure 1a,b, and Table S2 (Supporting Information) and selected area electron diffraction (SAED) patterns in Figure 1c,d can be assigned to a single space group, R-3m. There are no visible superstructure reflections from the C2/m Li_2MnO_3-like phase, indicating a random intralayer cation arrangement. The XRD data (Figure 1a,b) shows that the intensity of the (104) peak is significantly higher in reference to the (003) peak, and the (018) and (110) reflections overlap. These observations deviate from the typical diffraction of a R-3m structure, indicating the presence of partial disorder in both compounds. The refined lattice parameters in the R-3m space group are a = 2.9086(3) Å; c = 14.350(1) Å for LCT, and a = 2.9093(2) Å; c = 14.400(1) Å for LCT-HE. A c/a ratio close to 4.99 indicates that the structure is well-layered (e.g., as in $LiCoO_2$), while c/a = 4.90 is characteristic of cubic structures such as disordered rocksalt (DRX) or spinel.[49] LCT and LCT-HE have intermediate c/a values equal to 4.93 and 4.95, respectively. To determine the degree of cation mixing between Li^+ and other cations, appropriate constraints must be imposed (Note S2, Supporting Information) due to limitations of the XRD technique in terms of sensitivity toward Li.

© 2025 The Author(s). Advanced Energy Materials published by Wiley-VCH GmbH

16146840, 0, Downloaded from https://advanced.onlinelibrary.wiley.com/doi/10.1002/aenm.202502157, Wiley Online Library on [16/06/2025]. See the Terms and Conditions (https://onlinelibrary.wiley.com/terms-and-conditions) on Wiley Online Library for rules of use; OA articles are governed by the applicable Creative Commons License

We find that the mixing level for LCT-HE is slightly lower than that for LCT (15.2% and 17.2%, respectively), which, together with the higher c/a ratio (Table S2, Supporting Information), substantiates that LCT-HE is more layered-like. To gain insight into the local cation arrangement within the PD structure, we utilized high-resolution transmission electron microscopy (HR-TEM, Figure 1e,f), which is sensitive to phase contrast. For both samples, the degree of (dis)ordering is found to vary locally, from more ordered layered-like regions (yellow squares with the corresponding fast Fourier transform (FFT) indexed to the R-3m phase) to partially cation disordered regions (green squares, Fm-3m rocksalt features marked with green circles in FFT coexist with spots from the layered phase). Interestingly, regions with spinel-like ordering were also detected (Figure S1, Supporting Information). Presumably, these regions are similar to lithiated spinel ($Li_{2(16c)}M_{2(16d)}O_4$), which may coexist with both layered and DRX phases.[49–51] Such a lithiated spinel phase can be difficult to distinguish in powder XRD from a layered phase when the oxygen array is cubic-close-packed (c/a = 4.90).[49,51–53] Because the structures are distinguishable in single-crystal experiments,[53] they can be detected through HR-TEM. Since layered, spinel, and rocksalt structures can share the same oxygen framework and smoothly transform into each other on the scale of a few nanometers, LCT and LCT-HE are classified as single-phase PD layered oxides that locally exhibit different cation disorder (schematically shown in Figure 5a in the Discussion section). It should be noted that Rietveld refinement based on a two-phase model, including fully ordered layered (R-3m) and fully disordered (Fm-3m) phases, might initially seem more appropriate (see Note S2, Figure S2, and Table S2, Supporting Information). However, considering the range of disorder levels in the samples revealed by HR-TEM, which the two-phase model does not capture, the single-phase model more accurately represents the real structure of LCT and LCT-HE. Moreover, since using average structural parameters in a single-phase model makes interpretation more straightforward, we selected the single-phase approach (with an R-3m layered phase and refined cation mixing) to simplify the analysis and interpretation of the PD structure. The results of scanning transmission electron microscopy (STEM) with energy-dispersive X-ray spectroscopy (EDS) mapping (Figure 1g; Figure S3a, Supporting Information) show that the cations are distributed homogeneously with no segregation, further supporting that both materials should be treated as single-phase. Using scanning electron microscopy (SEM), the particle size for both samples was measured (Figure 1h; Figure S3b, Supporting Information). It varies from 300 nm up to 3 µm, which is generally smaller than for as-synthesized DRX materials (due to the lower synthesis temperature of 850 °C for PD oxides compared to 1000–1100 °C for Mn- and Cr-based DRXs[19,22,27]), but significantly larger than for ball-milled DRX samples, a process commonly done prior to the preparation of DRX-based electrodes to produce submicron secondary particles.[17,19,54]

2.2. Electrochemical Properties of Partially Disordered Oxides

The electrochemical performance of LCT and LCT-HE electrodes was evaluated using a galvanostatic cycling technique between 1.5–4.8 V and 2–4.4 V at 25 °C and at a current of 20 mA g^{-1}, with the results presented in **Figure 2**a,b. In the 1st discharge down to 1.5 V, LCT delivers a capacity of 223 mAh g^{-1} (689 Wh kg^{-1}), whereas LCT-HE delivers a higher value of 286 mAh g^{-1} (881 Wh kg^{-1}). Even though the tested electrodes were prepared using the as-synthesized PD materials, without additional nanosizing, the recorded capacities and energy densities are comparable with the best performing Mn- and Cr-based DRXs after high-energy ball milling[9,19,22,27] (see comparison in Table S3, Supporting Information). These results indicate that the Li^+ transport properties are improved in the PD structure compared with DRX, the origins of which will be explained in detail in the Discussion section. Reasonably high capacities can also be obtained when cycling in a narrower 2.0–4.4 V range, reaching 190 mAh g^{-1} (619 Wh kg^{-1}) and 226 mAh g^{-1} (727 Wh kg^{-1}) for LCT and LCT-HE, respectively. As evidenced by the voltage profiles (Figure 2a,b) and the galvanostatic intermittent titration technique (GITT, Figure S4a,b, Supporting Information), both materials do not exhibit significant voltage hysteresis (0.41 and 0.48 V for LCT and LCT-HE, respectively), far below that of other Cr-based Li-rich compounds such as $Li_{1.2}Cr_{0.4}Mn_{0.4}O_2$ (>2.5 V).[55] Based on the GITT data, the higher discharge capacities observed in the initial cycles for LCT-HE compared to LCT (Figure 2a–d) can be connected to the decreased overpotential related to mass transfer, especially during deep discharge (Figure S4c–e, Supporting Information). Another substantial difference between the two materials is capacity evolution (Figure 2c,d) and voltage retention (Figure 2e,f; Figure S5a,b, Supporting Information) during cycling. For LCT, the capacity increases from 223 to 259 mAh g^{-1} over the first 12 cycles between 1.5–4.8 V. Upon further cycling the capacity decreases with a similar slope as observed for LCT-HE (87.6% retention between 12th and 50th cycles for LCT, 86.2% for LCT-HE). The voltage profile evolution for LCT, illustrated in the normalized capacity plots for selected cycles (Figure 2e), shows a gradual formation of new pseudo-plateaus, centered at lower voltages during discharge and higher voltages during charge, thereby increasing the hysteresis. Figure 2g shows the average charge and discharge voltage as a function of cycle number. For LCT, a pronounced voltage fade occurs, with its asymmetrical character clearly visible in the rapid decrease in the average discharge, but not charge, voltage. Some changes in the voltage profiles can also be observed for LCT-HE (Figure 2f), but to a much smaller extent. Moreover, the average voltage changes are more symmetrical (Figure 2g). Similar but less pronounced phenomena for both materials are visible during cycling between 2.0–4.4 V (Figure S5, Supporting Information). Both PD compounds exhibit very high capacities even at currents as high as 1000 mA g^{-1} (Figure 2h; Figure S6a, Supporting Information), delivering 143 mAh g^{-1} (LCT-HE) and 142 mAh g^{-1} (LCT) in the 1st discharge between 1.5–4.8 V. Note that the values are comparable with $Li_{1.2}Cr_{0.2}Mn_{0.2}Ti_{0.4}O_2$ DRX (155 mAh g^{-1}),[22] but for the PD materials, they were achieved without extensive mixing with carbon and without decreasing the particle size through milling. The capacity retention trend observed at 20 mA g^{-1} is generally maintained under higher currents (Figure S6b,c, Supporting Information), but the capacity increase in the initial cycles for LCT becomes less pronounced. This is also valid for extended cycling up to 100 cycles within the narrower voltage window of 2–4.4 V (Figure S6d,e, Supporting Information; long-term cycling in the 1.5–4.8 V voltage range leads to intensified electrolyte

© 2025 The Author(s). Advanced Energy Materials published by Wiley-VCH GmbH

16146840, 0, Downloaded from https://advanced.onlinelibrary.wiley.com/doi/10.1002/aenm.202502157, Wiley Online Library on [16/06/2025]. See the Terms and Conditions (https://onlinelibrary.wiley.com/terms-and-conditions) on Wiley Online Library for rules of use; OA articles are governed by the applicable Creative Commons License

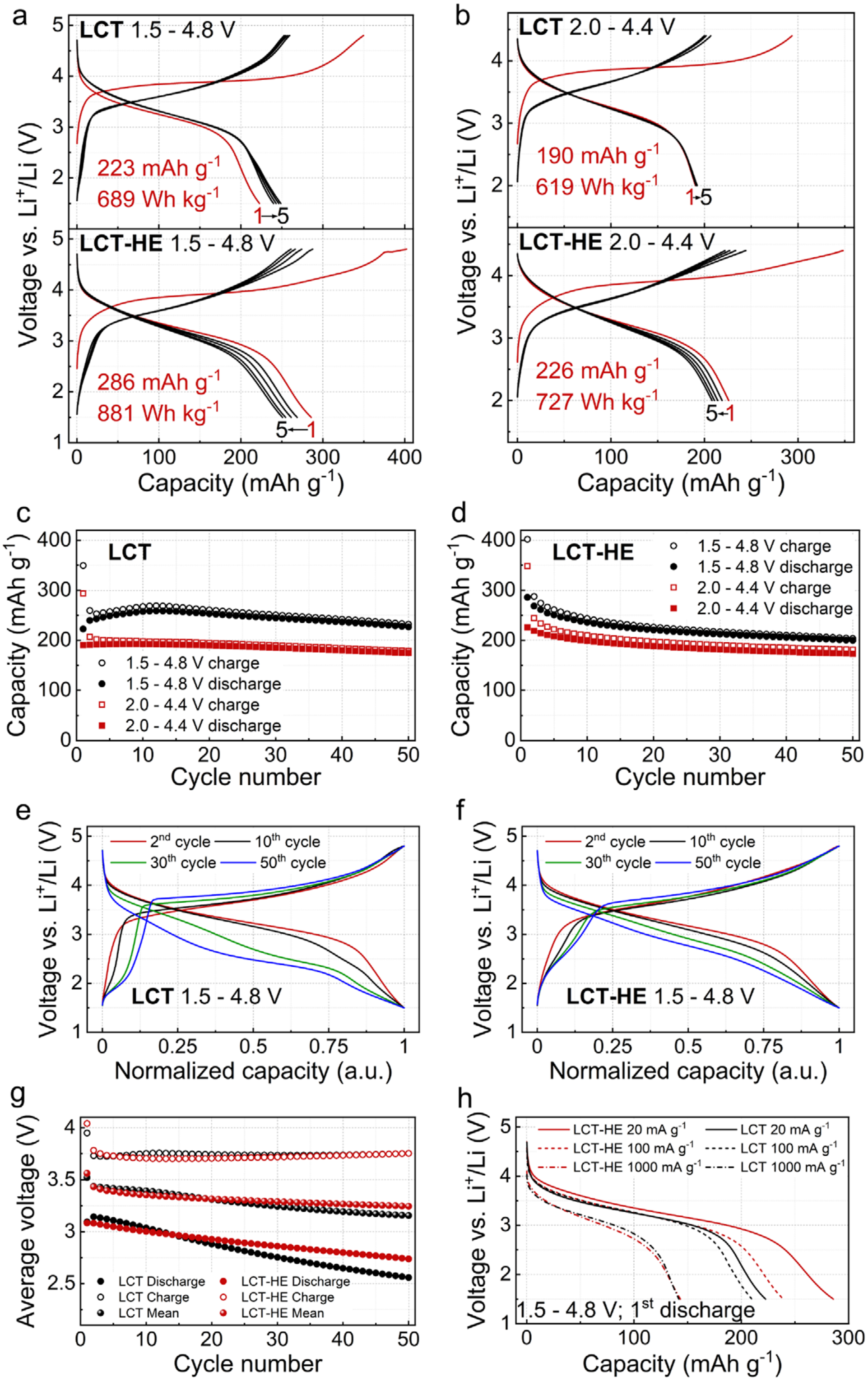

Figure 2. Electrochemical characterization. a,b) Voltage profiles for cycles 1–5 for LCT (top) and LCT-HE (bottom) at 20 mA g^{-1} cycled in the voltage range of 1.5–4.8 V (a) and 2.0–4.4 V (b). c,d) Capacity retention plots for LCT (c) and LCT-HE (d) cycled at 20 mA g^{-1} for 50 cycles between 1.5–4.8 and 2.0–4.4 V. e,f) Normalized voltage profiles for the 2nd, 10th, 30th, and 50th cycles cycled at 20 mA g^{-1} between 1.5–4.8 V for LCT (e) and LCT-HE (f). g) Average discharge and charge voltage evolution over 50 cycles for LCT and LCT-HE at 20 mA g^{-1} in the voltage range of 1.5–4.8 V. Mean values were calculated as (discharge voltage + charge voltage)/2. h) 1st discharge voltage profiles for LCT and LCT-HE cycled between 1.5-4.8 V at different currents.

© 2025 The Author(s). Advanced Energy Materials published by Wiley-VCH GmbH

16146840, 0, Downloaded from https://advanced.onlinelibrary.wiley.com/doi/10.1002/aenm.202502157, Wiley Online Library on [16/06/2025]. See the Terms and Conditions (https://onlinelibrary.wiley.com/terms-and-conditions) on Wiley Online Library for rules of use; OA articles are governed by the applicable Creative Commons License

decomposition). Interestingly, LCT and LCT-HE show a remarkably similar capacity at 1000 mA g^{-1} (only 1% difference), while the superiority of LCT-HE becomes increasingly evident at medium (100 mA g^{-1}, capacity higher by 13%) and low currents (20 mA g^{-1}, capacity higher by 22%). Therefore, there must be an additional, kinetically-limited Li^+ transport mechanism present only in LCT-HE, which becomes gradually deactivated with increasing current loads. The comparison of electrochemical results between LCT and LCT-HE indicates that introducing a high-entropy mixture, using less d^0 cation content, and shifting toward a more layered character of the PD oxide significantly impact the electrochemical performance. These changes lead to improved capacity at low and medium currents (while maintaining the same performance under high loads), a stable voltage profile, and reduced voltage fade during cycling for LCT-HE. The rate of capacity degradation observed upon cycling for both materials is similar to the behavior reported of many DRX compounds[8,27] and may be caused by TM dissolution and electrolyte breakdown, which are intensified by cycling in a wide voltage window. To explain our observations of better Li^+ transport properties in the PD structure compared to DRXs, as well as to understand the differences in the electrochemical properties of LCT and LCT-HE, we will thoroughly study the redox mechanisms, structural changes upon cycling, and TM migration for both materials in the following sections.

2.3. Redox Mechanism

The TM redox mechanism for LCT and LCT-HE was studied by hard X-ray absorption spectroscopy at the relevant metal K-edges (hXAS) and supported by soft XAS at L_3-edges (sXAS). Cr K-edge X-ray absorption near structure (XANES) spectra for the pristine, top of charge, and bottom of discharge samples in the 1st cycle between 1.5–4.8 and 2.0–4.4 V, together with the spectra measured for selected standards, are presented in **Figure** 3a,b. The oxidation state of Cr can be estimated from the rising edge energy (corresponding to the excitation from 1*s* to 4*p* orbitals) and the pre-edge intensity (related to 1*s* to 3*d* transitions[55,56]) and comparing them with standards. The very high intensity of the pre-edge peak in the CrO_3 standard is characteristic of tetrahedral Cr^{6+} coordination, which enables a high probability of 1*s* to 3*d* transitions due to hybridization between Cr 3*d* and O 2*p* orbitals.[55,56] Therefore, the pre-edge intensity ratio between the measured spectra and the CrO_3 standard can be used to estimate the content of tetrahedral Cr^{6+} present in the samples (Figure 3c). In the pristine state, Cr K-edges for LCT and LCT-HE are similar and close to the $LiCrO_2$ standard, indicating the presence of Cr^{3+}. Upon delithiation, the edge energy shifts from 5998 eV to 6007 and 6006 eV for LCT and LCT-HE, respectively. The intensity of the pre-edge at ca. 5993 eV also increases significantly in both samples, indicating Cr oxidation and migration. Most of Cr^{3+} in LCT is oxidized to Cr^{6+} and migrates to tetrahedral sites at the top of charge, while it is relatively less oxidized in LCT-HE. There is almost no change in the XANES spectra for both compounds when charging from 4.4 to 4.8 V, indicating that the capacity delivered above 4.4 V is not primarily due to Cr oxidation. Upon discharge to 2.0 or 1.5 V, the edge energy for both materials shifts back close to 5998 eV, similar to the $LiCrO_2$ reference, but remains at slightly higher energy than in the pristine state. This suggests the presence of mostly octahedral and trivalent Cr at the end of discharge, but with some Cr at higher oxidation state. Noticeably, LCT still exhibits a pronounced pre-edge peak intensity after discharge, which is more intense than in the CrO_2 reference spectrum (Figure 3c) and therefore may be attributed to the presence of remaining Cr^{6+} rather than Cr^{4+} (although it is difficult to determine whether small quantities of Cr^{4+} exist in addition to mostly Cr^{3+} and Cr^{6+}). More Cr^{6+} remains at the end of discharge when cycling within the wider voltage range, as evidenced by the more intense pre-edge peak after discharge to 1.5 V compared to 2.0 V (Figure 3a). On the other hand, the pre-edge intensity for LCT-HE after discharge does not exceed that of the CrO_2 reference. This suggests a more complete reduction for LCT-HE, with consistent behavior in both voltage ranges (2.0–4.4 and 1.5–4.8 V), unlike LCT which shows different behavior in these ranges. To further probe the valence of Cr, we measured the mapping of resonant inelastic X-ray scattering (mRIXS) at the Cr L_3-edge and derived the inverse partial fluorescence yield (iPFY) spectra (Figure S7 and Note S3, Supporting Information), which provide an undistorted direct probe of the 3*d* valence states.[57] These sXAS results further support the incomplete oxidation of Cr^{3+} to Cr^{6+} in both materials, as the measured iPFY spectra in the fully charged state still exhibit the signal related to Cr^{3+} (Figure S7e, Supporting Information), and the characteristic dd excitation peaks (which d^0 Cr^{6+} does not possess) are still visible in the RIXS spectra (Figure S7g, Supporting Information). Additionally, based on the peak intensity differences in mRIXS and iPFY between LCT and LCT-HE, less Cr oxidation is taking place for LCT-HE, consistent with the hXAS data. The measured K-edge XANES and L_3-edge sXAS spectra for the other cations in the samples confirm that the initial oxidation states are close to the targeted Ti^{4+}, Fe^{3+}, and Mo^{6+} and that these are redox inactive within the tested voltage windows (Figures S8–S10 and Note S3, Supporting Information). However, Mn in LCT-HE appears to exhibit an oxidation state lower than the targeted 4+. This may be caused by Mn reduction during the synthesis in an inert atmosphere. The sXAS measured in total electron yield mode (Figure S9c, Supporting Information) shows that the effect is especially pronounced on the surface. The observed change in the spectrum shape at the Mn L_3-edge upon charge (Figure S9d, Supporting Information) and the small shifts in the Mn K-edge (toward lower energy upon discharge and higher energy upon charge compared to the pristine state, Figure S10c, Supporting Information) suggest partial redox activity of the $Mn^{3+/4+}$ pair. However, taking into account the low content of Mn in LCT-HE, its contribution to the overall capacity is negligible, certainly below 16 mAh g^{-1} (which would be the case for complete $Mn^{3+/4+}$ redox on all constituent Mn). Based on the literature reports for Al-containing layered Li oxides, Al is assumed to be in the 3+ oxidation state and redox inactive.[48,49,58] The XANES studies show that Cr is the main redox active TM for both LCT and LCT-HE. The compositions of LCT and LCT-HE were designed to extract all 1.2 mol of Li if the full oxidation of Cr from 3+ to 6+ can be achieved without O redox, yielding theoretical capacities of 401 mAh g^{-1} (LCT) and 390 mAh g^{-1} (LCT-HE). However, according to the linear combination fitting of Cr L_3-edge iPFY spectra with reference spectra (see Figure S7e,f and Note S3, Supporting Information), the redox of the $Cr^{3+/6+}$ pair is incomplete (ca. 73% of Cr^{6+} in

© 2025 The Author(s). Advanced Energy Materials published by Wiley-VCH GmbH

16146840, 0, Downloaded from https://advanced.onlinelibrary.wiley.com/doi/10.1002/aenm.202502157, Wiley Online Library on [16/06/2025]. See the Terms and Conditions (https://onlinelibrary.wiley.com/terms-and-conditions) on Wiley Online Library for rules of use; OA articles are governed by the applicable Creative Commons License

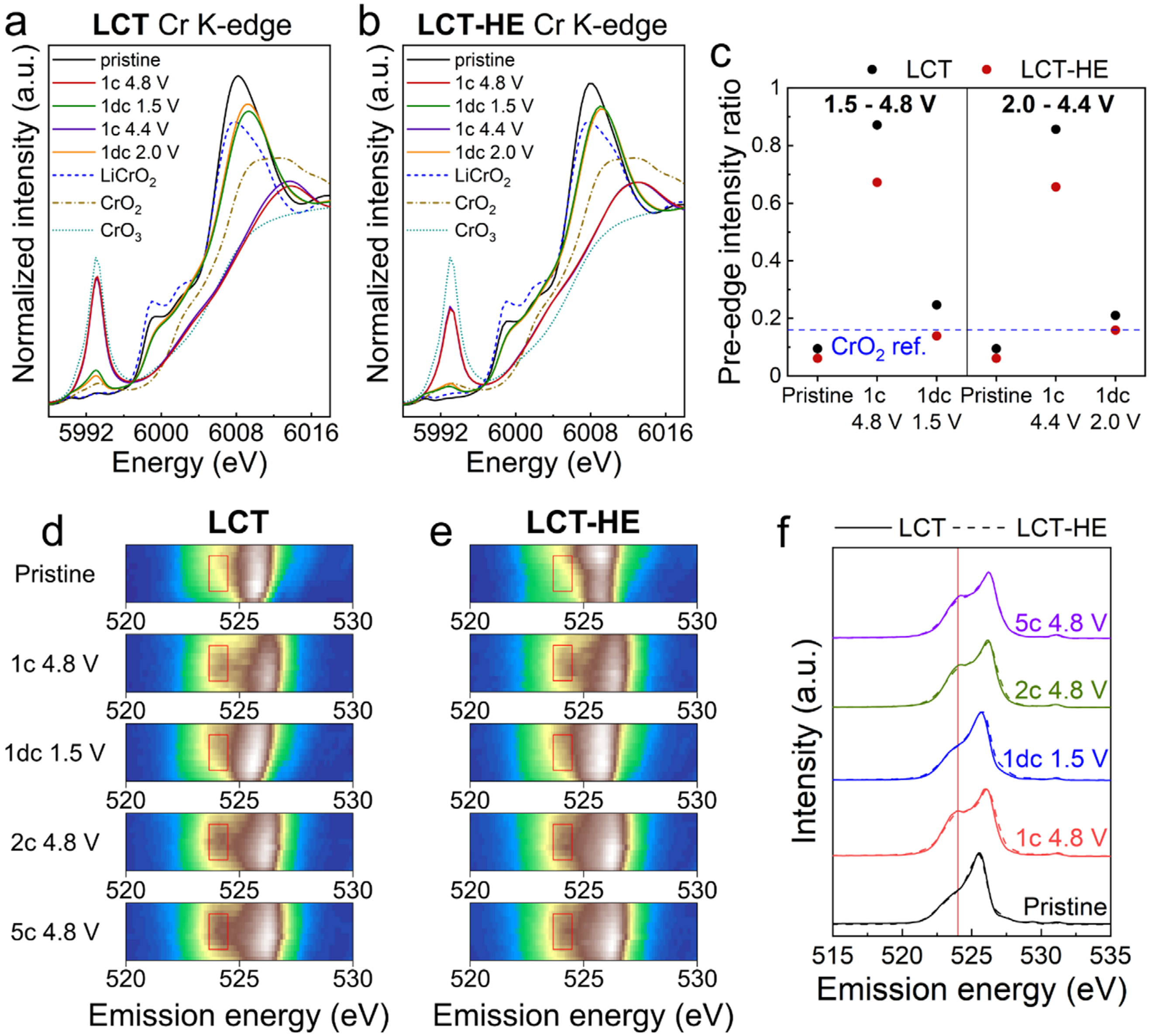

Figure 3. Redox mechanism study. a,b) Cr K-edge XANES spectra for LCT (a) and LCT-HE (b) for the pristine samples and the samples (dis)charged between 1.5–4.8 and 2.0–4.4 V. The spectra for $LiCrO_2$, CrO_2, and CrO_3 references are plotted as dashed lines. c) The intensity of the pre-edge peak at ca. 5993 eV normalized by the intensity of the CrO_3 standard for LCT and LCT-HE cycled between 1.5–4.8 V and 2.0–4.4 V. Also plotted is the intensity ratio of the CrO_2/CrO_3 standards. d,e) O K-edge mRIXS for the selected samples, including pristine, the top of charge (4.8 V) after the 1st, 2nd, and 5th cycles, and the bottom of discharge (1.5 V) after the 1st cycle for LCT (d) and LCT-HE (e). The excitation energy window along the vertical axis is between 530 and 532 eV. The red boxes mark the energy region for the oxygen redox feature. f) Integrated RIXS cuts around the selected 531 eV excitation energy at different (dis)charge steps. Solid lines correspond to LCT and dashed lines correspond to LCT-HE. The peak at the emission energy of ca. 523.7 eV marked with the red line is characteristic for oxidized oxygen.

LCT and 51% in LCT-HE after the 1st charge to 4.8 V). Since a substantial amount of capacity is delivered above 4.4 V, part of the charge compensation is expected to occur through O redox. To investigate this, we utilized mRIXS for O K-edge, which overcomes the limitations of conventional O K-edge XAS and is therefore often selected to characterize O redox in Li-excess cathode materials.[19,27,59,60] The feature characteristic for oxidized oxygen can be detected at the excitation energy of ca. 531 eV and the emission energy of ca. 523.7 eV.[19,27,59,60] Figure 3d,e shows the ex-situ O-K RIXS maps for LCT and LCT-HE at the selected points in cycling. The red boxes mark the energy region of the oxidized oxygen feature, which is clearly visible at the top of charge after the 1st, 2nd, and 5th cycles, and disappears after full discharge to 1.5 V. Both LCT and LCT-HE show similar O redox behavior as shown in RIXS cuts around the 531 eV excitation energy (Figure 3f). After the 1st cycle, the intensity of the O redox peak is decreased in the 2nd charge but is then stable in subsequent cycles. Also, upon discharging to 1.5 V, the peak intensities are

© 2025 The Author(s). Advanced Energy Materials published by Wiley-VCH GmbH

16146840, 0, Downloaded from https://advanced.onlinelibrary.wiley.com/doi/10.1002/aenm.202502157, Wiley Online Library on [16/06/2025]. See the Terms and Conditions (https://onlinelibrary.wiley.com/terms-and-conditions) on Wiley Online Library for rules of use; OA articles are governed by the applicable Creative Commons License

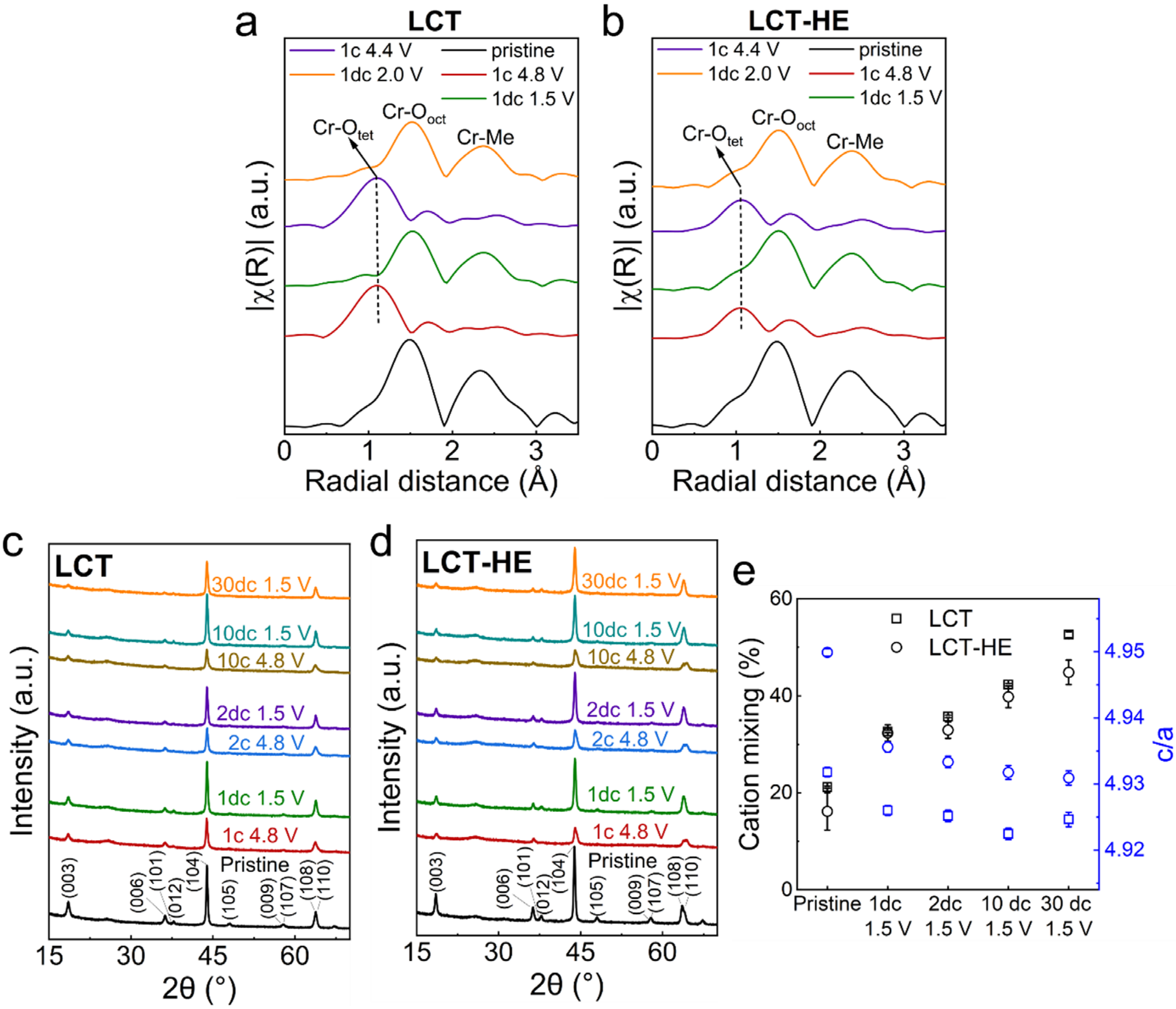

Figure 4. Cation migration and structural changes upon cycling in the PD oxides. a,b) k^2-weighted Fourier transformed Cr K-edge EXAFS spectra for LCT (a) and LCT-HE (b) for the pristine samples and the samples (dis)charged between 1.5–4.8 or 2.0–4.4 V. The peaks centered at ca. 1.0, 1.5, and 2.5 Å are assigned to CrO_4 tetrahedral coordination (Cr-O$_{tet}$), CrO_6 octahedral coordination (Cr-O$_{oct}$), and the interactions of Cr with other cations in the second shell (Cr-Me), respectively, in line with previous reports.[22,55,65] The Fourier transformed spectra are not phase corrected, so the actual distances should be ca. 0.3–0.4 Å longer.[22] c,d) Ex situ XRD patterns measured for electrodes with LCT c) and LCT-HE d) for the pristine samples, at the top of charge and bottom of discharge after 1, 2, 10, and 30 cycles between 1.5–4.8 V. e) Evolution of the degree of cation mixing and c/a ratio upon cycling for the fully lithiated LCT and LCT-HE. The parameters were calculated from the Rietveld refinement.

similar to those of the pristine samples. Hence, the O redox exhibits good reversibility on cycling, complementing $Cr^{3+/6+}$ redox, contrary to many previously reported Li-excess layered cathodes where excessive O redox occurs and is irreversible.[5,42,61]

2.4. Structural Changes and Cation Migration

None of the investigated K-edges of the redox-active ions is fully recovered after discharge as compared to the pristine state. In all but the case of Cr, these changes are mainly to the shape of the edge rather than the energy of the edge, suggesting changes in the local arrangements around cations. Because the Cr^{6+} formed upon charge is stable only in tetrahedral coordination,[62] it is believed that it must migrate during the electrochemical process in order to be oxidized. To precisely characterize the local structural changes and Cr migration on (dis)charge, we utilized extended X-ray absorption fine structure (EXAFS) spectroscopy. Upon charging to 4.4 and 4.8 V, a new peak centered at a lower R (ca. 1.0 Å in uncorrected phase scale) emerges in the Cr K-edge EXAFS spectra for LCT and LCT-HE (**Figure** 4a,b), paired with a simultaneous decrease in the intensity of the peak corresponding to Cr-O$_{oct}$ bonds. Because the bonds in $Cr^{6+}O_4$ coordination are short, this new feature can be assigned to Cr-O$_{tet}$[55] and confirms that Cr moves from its original octahedral position to tetrahedral sites. There is less tetrahedral occupation in LCT-HE, consistent with the less extensive Cr oxidation detected from XANES. Also, there are no changes in the EXAFS spectra for LCT-HE

© 2025 The Author(s). Advanced Energy Materials published by Wiley-VCH GmbH

16146840, 0, Downloaded from https://advanced.onlinelibrary.wiley.com/doi/10.1002/aenm.202502157, Wiley Online Library on [16/06/2025]. See the Terms and Conditions (https://onlinelibrary.wiley.com/terms-and-conditions) on Wiley Online Library for rules of use; OA articles are governed by the applicable Creative Commons License

between 4.4 and 4.8 V (Figure S11, Supporting Information), while for LCT it is found that Cr further migrates to a small extent. On discharge, the amplitude increases for the Cr-O_{oct} peak and decreases for the Cr-O_{tet} for both studied materials. This indicates that Cr migrates back to the octahedral sites upon reduction. However, the amplitude of the Cr-O_{oct} peak is lower than that in the pristine samples. This result can be correlated with the pre-edge peak intensity dependence analysis from XANES (Section 2.3. and Figure 3c), together suggesting that some $Cr^{6+}O_4$ coordination remains present at the bottom of discharge, especially in LCT. We also performed EXAFS studies for other cations in the samples, with the detailed analysis provided in Note S4 (Supporting Information) and Figure S12 (Supporting Information). Ti in LCT and Ti, Mn, Fe, and Mo in LCT-HE were confirmed to be immobile and stable in octahedral sites. We interpret the observed minor changes in the EXAFS spectra of these other elements as originating from the local structural distortions due to Cr migration. We also find that these distortions around the investigated absorbers on charge remain present on discharge with most of them accumulated around Ti in LCT and around Ti and Mo in LCT-HE, consistent with the ability of fully oxidized d^0 cations to more easily accommodate distortion.[10]

To investigate the influence of Cr mobility on more global structural changes, we utilized ex-situ XRD measurements. Figure 4c,d and Figure S13 (Supporting Information) show the patterns measured for the fully charged and discharged samples after a different number of cycles. At every stage of charge, LCT and LCT-HE can be assigned to the initial single-phase PD structure (R-3m space group). However, the variations in the relative intensity of reflections indicate dynamic changes in cation mixing. After the 1st charge, the intensity of all peaks has decreased for both materials as compared to the pristine electrodes (similar active material mass), with some of them almost completely disappearing ((101)/(012) peaks at ca. 38°, (015) peak at ca. 48°, (009)/(107) peaks at ca. 58°). The intensity decrease of these specific peaks is consistent with Cr migration to tetrahedral positions.[55] All reflections are broader for LCT-HE in comparison to LCT, suggesting that larger distortions are present in the material. Also, the structure of LCT-HE remains more layered-like, as evidenced by the better separation of the (018) and (110) peaks at ca. 64° (see the magnified patterns in Figure S14, Supporting Information). Similar features can be observed in the patterns measured after the 2nd, 10th, and 30th charge to 4.8 V. After the 1st discharge, the intensity of the peaks for both samples is regained but not to the same level as in the pristine state. In particular, the relative intensity of the (003)/(104) peaks (ca. 18° and 44°) is lower. Therefore, while most of Cr has migrated back to octahedral positions upon full discharge, the degree of cation mixing remains greater than the pristine samples. The most significant changes (in the fully lithiated state) can be observed when comparing the pristine state to the sample after the 1st cycle in both compounds. This is consistent with the irreversible character of the 1st charge voltage profile (Figure 2a,b) and the decreased intensity of the O redox peak between the 2nd and 1st charge (Figure 3c–e). We used Rietveld refinement to calculate the level of cation mixing and the c/a ratio, and to track their evolution upon cycling (Figure 4e). The details of Rietveld fitting are provided in Note S2 (Supporting Information), with representative refinements shown in Figure S15 and Table S4 (Supporting Information). In the consecutive charge/discharge cycles, the cation mixing increases and the c/a ratio decreases, leading to more disordered samples. Both parameters taken together indicate that LCT-HE is initially more layered-like than LCT and remains this way during cycling. The level of cation mixing increases between the 1st discharge and 30th discharge from 33(1)% to 53(1)% for LCT, and from 32(2)% to 45(3)% for LCT-HE. The larger increase in the degree of disorder for LCT is likely the result of its greater extent of Cr migration. Interestingly, the ex-situ XRD patterns after the 10th and 30th discharge are similar for LCT-HE, whereas for LCT, the peak intensity after the 30th discharge is lower compared to the 10th discharge (the active material mass in the electrodes was similar for the cells cycled for 10 and 30 cycles, so it should not influence the intensity that much). Additionally, after the 30th discharge, some of the reflections for LCT have almost no intensity (at ca. 38°, 48°, and 58°). The loss of intensity in these reflections is similar to the features observed after the 1st charge to 4.8 V, which are characteristic of tetrahedral Cr occupancy. It is, therefore, possible that a greater accumulation of Cr-O_{tet} in LCT is responsible for the visible differences in the XRD data between the samples after 30 cycles. This suggests that the trapping of Cr^{6+} in tetrahedra after the 1st discharge in LCT, detected by Cr K-edge XANES, also occurs in subsequent cycles, leading to the accumulation of trapped Cr^{6+}. In contrast, this phenomenon is not present in LCT-HE to the same extent, as evidenced locally by XAS and globally by XRD. The lattice parameter evolution during cycling indicates that both materials undergo very small volume changes, similar to some other DRX materials which are labeled "zero-strain" (Figure S16, Supporting Information).[7,23,63,64] During the 1st discharge from 4.8 to 1.5 V, the volume change is only 0.3% for LCT and 0.6% for LCT-HE.

3. Discussion

3.1. Li^+ Transport in the Partially Disordered Structure

The electrochemical results presented in this work clearly show that the designed PD oxides are based on $Cr^{3+/6+}$ and highly reversible O redox and exhibit better Li^+ transport properties than typical DRX materials, enabling them to be used as cathode materials in their as-synthesized form, with particle sizes above 1 µm. We attribute this to the combination of 0-TM and 1-TM channels in the PD layered structures. While 0-TM are only formed in layered structures when Li excess or partial disorder is introduced,[7,10] the larger separation between the 111 planes that create the Li-slab in a layered structure activates the 1-TM channels in them, enabling them to participate in Li^+ diffusion.[7] We hypothesize that in PD oxides the predominant Li^+ transport occurs through 0-TM channels, while the additional accessible 1-TM jumps contribute to the overall connectivity of the percolation network. Our materials stand in contrast to Cr-containing well-ordered layered oxides, such as $Li_{1.2}Cr_{0.4}Mn_{0.4}O_2$[55,65] and $Li_{1.2}Cr_{0.2}Co_{0.2}Mn_{0.4}O_2$,[66] which exhibit large voltage hysteresis.[55] Consistent with recent work[55] demonstrating that a certain level of disorder needs to be introduced into the structure of Cr-based cathodes to mitigate the hysteretic behavior, the voltage hysteresis for our materials is below 0.5 V (Figure S4a,b, Supporting Information). As evidenced by the TEM analysis in Section 2.1 (Figure 1e,f), the local cation

© 2025 The Author(s). Advanced Energy Materials published by Wiley-VCH GmbH

16146840, 0, Downloaded from https://advanced.onlinelibrary.wiley.com/doi/10.1002/aenm.202502157, Wiley Online Library on [16/06/2025]. See the Terms and Conditions (https://onlinelibrary.wiley.com/terms-and-conditions) on Wiley Online Library for rules of use; OA articles are governed by the applicable Creative Commons License

arrangement in LCT and LCT-HE varies. In the as-synthesized material, we experimentally observe both more ordered layered-like environments which are integrated with more cation-mixed (sometimes spinel-like) regions without abrupt phase boundaries and with no clear domain structure. This variability is enabled by the fact that all these structures share the same oxygen sublattice, while the materials themselves exhibit a homogeneous composition (Section 2.1 and Figure 1g). These different cation orderings result in varying Li^+ transport properties, creating a unique and complex diffusion network. In more layered-like regions, Li^+ diffusion through 1-TM channels should have a relatively low migration barrier, making them active, whereas in disordered and spinel-like regions, jumps through 0-TM channels are more facile. **Figure** 5a illustrates the proposed description of the PD layered structure. Moreover, as we demonstrated, $Cr^{3+/6+}$ redox not only provides a large TM redox reservoir but also coincides with the migration of Cr to tetrahedral sites, possibly further improving Li^+ kinetics by creating new 0-TM and/or 1-TM channels (by transforming from 1-TM or 2-TM channels), as has been argued for $Li_{1.2}Cr_{0.2}Mn_{0.2}Ti_{0.4}O_2$.[22] We believe that it is this mixed 0-TM/1-TM network, combined with the large amount of mobile Cr, that allows PD materials to outperform traditional DRXs in terms of Li^+ diffusivity and work effectively in the as-synthesized form.

3.2. Role of Chemical Composition in the Partially Disordered Oxides

Recent studies show that as-synthesized $Li_{1.2}Cr_{0.4}Mn_{0.4}O_2$ forms an ordered layered structure[55,65] and requires ball milling to introduce partial disorder.[55] This is because the material contains only TMs with occupied *d* orbitals and that have a large mismatch of ionic radii with Li^+, both factors which favor ordering.[10,67] When trying to synthesize disordered rocksalts, incorporating more than ca. 0.2 Cr per formula unit typically leads to the formation of an electrochemically inactive $LiCrO_2$ secondary phase (within a reasonable temperature range)[22,27,29,68] unless non-equilibrium synthesis methods, e.g. mechanochemical synthesis, are utilized.[69–71] In contrast, in LCT and LCT-HE, the combination of layered- and DRX-forming elements enables the direct formation of a PD structure through a solid-state route. Additionally, a high content of Cr can be incorporated (0.4 per formula unit in the studied materials). Even though in both LCT and LCT-HE the main redox active cation is Cr and the materials differ only by 0.2 Ti^{4+} in LCT substituted by a high-entropy mixture in LCT-HE, they exhibit markedly different electrochemical performance. In particular, the energy density is higher, and the voltage profiles are more stable for LCT-HE.

To understand these differences, we start by discussing the evolution of the voltage profiles in our materials. In general, voltage fade may arise from a combination of two overlapping phenomena: 1) polarization growth where the mean voltage remains stable[9,21] (e.g., caused by electrolyte decomposition and TM dissolution[7,9,21]), and 2) structural changes causing an asymmetrical change in average charge and discharge voltage. The more asymmetrical voltage evolution for LCT (Section 2.2 and Figure 2e,g) suggests that the more pronounced voltage fade, compared to that of LCT-HE, is mainly of structural origin. The ex-situ structural studies demonstrate that LCT-HE undergoes less Cr^{3+} oxidation and migration to tetrahedral positions upon charging, while upon discharging, Cr^{6+} reduction and migration back to octahedral sites are more complete. We explain these phenomena by the difference in the capability of the other ions to accommodate strain induced by Cr mobility, schematically illustrated in Figure 5b. In LCT, the high content of d^0 Ti^{4+}, which can easily tolerate distortions to the octahedra it occupies,[13,41] allows for undisrupted oxidation and migration of Cr. It has been previously shown that once Cr^{6+} occupies a tetrahedral site, the adjacent Li^+ also moves to a tetrahedral position, forming a Cr_{tet}-Li_{tet} dumbbell, which lowers the overall energy of the system.[55,72] When in high concentration, these dumbbells interact through their strain fields, creating cooperative distortions. The high stability of these dumbbells makes them hard to break up during lithiation, leaving remnant oxidized Cr^{6+} in the structure, even after discharge to 1.5 V. During prolonged cycling, especially in a wide voltage range where the formation of dumbbells is intensified, they may accumulate, causing the average voltage to increase during charging and decrease during discharging (Section 2.2. and Figure 2e,g). After a sufficient number of cycles, the recorded voltage profiles somewhat resemble the highly hysteretic behavior reported for layered $Li_{1.2}Cr_{0.4}Mn_{0.4}O_2$,[55,65] even though the disorder needed to disrupt collective Cr migration[55] is present in LCT. Therefore, while reversible Cr migration during cycling increases disorder, irreversible migration and Cr_{tet}-Li_{tet} dumbbell formation could play a more significant role in driving hysteresis growth. In the initial cycles, when some Cr_{tet}-Li_{tet} dumbbells are already trapped but not yet accumulated in large amounts, the small numbers of Cr-O_{tet} might improve the percolation network by creating additional accessible diffusion channels,[22] which would explain the observed capacity increase up to the 12th cycle (Figure 2c). In contrast, due to the presence of more cations with occupied *d* orbitals that cannot easily accommodate distortions,[41] significant local strain appears in LCT-HE upon charging, reaching a point where further oxidation and migration of Cr become energetically unfavorable and cannot continue. Because fewer Cr_{tet}-Li_{tet} dumbbells form during charging, the subsequent reduction is more complete, resulting in fewer of them remaining stable in the structure. The enhanced Li^+ transport kinetics in LCT-HE, especially at the end of discharge (see GITT analysis in Section 2.2 and Figure S4, Supporting Information), likely also facilitates a more reversible Cr redox process. This explains the more stable evolution observed in the voltage profile of LCT-HE (Figure 2e,f). We note that it should be possible to force more (or even all) Cr^{6+} to be reduced and moved back to octahedral sites, even for LCT. However, this would require either discharging to voltages below 1.5 V (similar to what was reported for layered $Li_{1.2}Cr_{0.4}Mn_{0.4}O_2$ when discharging to 1.0 V[65]), or increasing the accessible discharge capacity without lowering the cutoff voltage (as demonstrated in the work on partially disordered $Li_{1.2}Cr_{0.4}Mn_{0.4}O_2$[55] or by further improving Li^+ kinetics).

In light of the above discussion, we can now address the remaining differences in the electrochemical properties between LCT-HE and LCT. Due to the lower amount of cation migration, the initially more layered-like LCT-HE maintains a more ordered structure during cycling, resulting in more facile 1-TM diffusion. Furthermore, the presence of multiple cations of different sizes

© 2025 The Author(s). Advanced Energy Materials published by Wiley-VCH GmbH

16146840, 0, Downloaded from https://advanced.onlinelibrary.wiley.com/doi/10.1002/aenm.202502157, Wiley Online Library on [16/06/2025]. See the Terms and Conditions (https://onlinelibrary.wiley.com/terms-and-conditions) on Wiley Online Library for rules of use; OA articles are governed by the applicable Creative Commons License

16146840, 0, Downloaded from https://advanced.onlinelibrary.wiley.com/doi/10.1002/aenm.202502157, Wiley Online Library on [16/06/2025]. See the Terms and Conditions (https://onlinelibrary.wiley.com/terms-and-conditions) on Wiley Online Library for rules of use; OA articles are governed by the applicable Creative Commons License

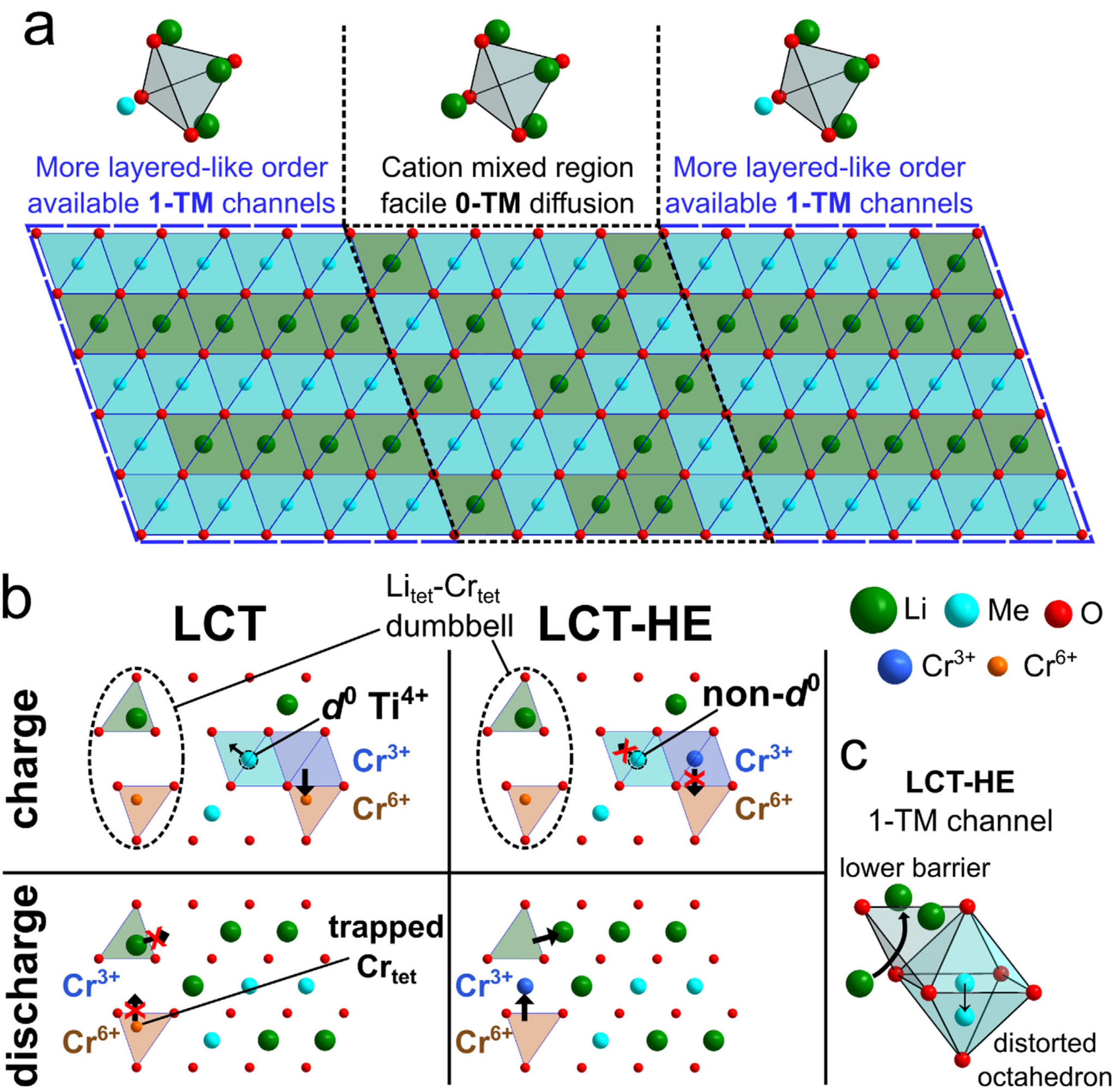

Figure 5. Schematic of PD structure and proposed Cr migration mechanism. a) The structure of a PD layered oxide. The FCC oxygen framework remains unchanged upon partial disordering, but the cation disorder creates a mixed 0-TM/1-TM diffusion network. b) Proposed explanation of the different reaction mechanisms in LCT and LCT-HE. During charge (top panel), oxidized Cr migrates to tetrahedral sites, coupled to the formation of Cr_{tet}-Li_{tet} dumbbells which stabilize the structure. In LCT, the high content of d^0 Ti^{4+} accommodates the distortions induced by the Cr oxidation and migration. In contrast, this process is at some point blocked in LCT-HE by the non-d^0 cations which are less accommodating to distortion. As a result, upon discharge (bottom panel), more Cr_{tet}-Li_{tet} dumbbells remain stable in LCT. The more irreversible reaction mechanism in LCT causes an accumulation of dumbbells upon cycling, further lowering energy and leading to increasingly hysteretic behavior. c) Decreased Li^+ jump barrier through a 1-TM channel due to distortions likely present in LCT-HE because of the variety of cation sizes. “Me” in the legend stands for any metal.

results in large local distortions in LCT-HE, which may alter the distribution of migration barriers,[13,44] an effect that has been observed in distorted high-entropy solid electrolytes.[44] Moreover, 1-TM diffusion can be partially activated through sufficient distortions in DRX cathodes by reducing the Li^+ migration barrier, which occurs when a TM cation shifts farther away from the activated tetrahedral site,[13] as may be the case for LCT-HE, as depicted in Figure 5c. These additional 1-TM channels might extend the percolation network only at lower currents and gradually become kinetically deactivated under higher loads, causing the amount of accessible Li^+ to eventually reach the same level as in LCT (see the discussion about rate performance in section 2.2.

© 2025 The Author(s). Advanced Energy Materials published by Wiley-VCH GmbH

and Figure 2h). What may make these 1-TM channels inaccessible at higher currents is their relatively higher migration barrier, resulting from the distorted local environment that may be present in LCT-HE, though a more detailed analysis would require extensive modeling with Molecular Dynamics or Kinetic Monte Carlo. To support our findings and interpretation, we synthesized another single-phase PD oxide (Figure S17a, Supporting Information), $Li_{1.2}Cr_{0.4}Ti_{0.3}Mn_{0.1}O_2$ (LCTM), in which 0.1 of d^0 Ti^{4+} in LCT was substituted by the layered-forming Mn^{4+}, resulting in the same content of layered-forming elements as in LCT-HE. Importantly, this approach does not introduce a high-entropy mixture, so the influence of distortions resulting from such a mixture on the accessible Li^+ content which we suggested for LCT-HE should not be present for LCTM. Figure S17 (Supporting Information) shows the obtained electrochemical results. As expected, the initial capacity and energy density for LCTM are higher than those for LCT, while the voltage profiles are highly stable, showing no significant signs of increasing voltage hysteresis. The capacity retention is similar to that of LCT-HE and does not exhibit the increase seen in the initial cycles for LCT. At the same time, the amount of accessible Li^+ in LCTM is lower than that in LCT-HE, demonstrating the positive impact of the mixture of multiple cations on the improved percolation network.

3.3. Remaining Challenges

This paper presents new perspectives on developing partially disordered oxides with good Li^+ transport properties and lower voltage hysteresis, without the need for high-energy ball milling. The primary challenge remaining for these materials is to improve their capacity retention. We note that while the similar capacity retention between LCT and LCT-HE suggests a common degradation mechanism (starting from the 12th cycle, see Section 2.2. and Figure 2c,d), the capacity fade for LCT-HE might be intensified by the potentially higher TM dissolution. This could be due to the replacement of stable Ti^{4+} with TMs prone to dissolution, such as Fe^{3+} and Mo^{6+}.[73,74] Improvement in capacity retention could be achieved by limiting metal dissolution, which is known to be a substantial problem for cathode materials with mobile cations,[7,21,55,74,75] e.g., by adjusting the electrolyte[55,74] or using particle coatings.[7,75] Limiting the relatively wide applied voltage range can also inhibit degradation (see the results for the 2.0–4.4 V cycling range, Figure 2b; Figure S5, Supporting Information). However, the challenge is to use this strategy without sacrificing too much energy density, which could be achieved by further improving Li^+ transport kinetics and reducing hysteresis. It remains an open and interesting question whether this can be achieved by further tuning the disorder level and limiting cation migration (excessive cation mixing likely worsens kinetics by raising the migration barrier through 1-TM channels[7,10]) through optimizing the content of d^0 and/or mobile ions. To better understand the diffusion network in the PD structure, further investigations are needed to quantify the amount of 0-TM and 1-TM channels and their specific contributions to Li-ion transport as was done for Li-V-O DRX materials.[11] Next, the evolution of this network should be studied in detail during long-term cycling, as it is expected to be influenced by the increasing disorder due to Cr mobility (Figure 4e). Limiting the extent of cation mixing during cycling to levels closer to those of the pristine material may be a promising strategy for further enhancing both the capacity and voltage stability of PD cathodes. Additional insight into the redox mechanism (specifically the extent of Cr and O redox and their reversibility) as a function of the extent of disorder and TM dopants would also be beneficial for the future design of PD oxides. Other opportunities for improvement can exist in the optimization of synthesis conditions and particle morphology, including size, shape, and distribution.

4. Conclusion

The partially disordered oxides designed in this work exhibit improved Li^+ transport properties compared to fully cation-disordered cathodes. This improvement is possible due to their improved 0-TM percolation and, most importantly, the activation of 1-TM channels in the more layered-like regions, resulting in an extended 0-TM/1-TM diffusion network that benefits Li^+ diffusivity and high capacity. We demonstrated that the presence of d^0 cations is necessary to form the PD structure during the synthesis. The resulting structure has enough disorder to disrupt collective Cr migration, which would otherwise lead to substantial voltage hysteresis. On the other hand, the presence of only d^0 redox inactive elements allows for extensive Cr migration, resulting in the trapping of Cr^{6+} in tetrahedral positions and eventually giving rise to voltage hysteresis after several cycles. To prevent that, we partially replaced Ti^{4+} in LCT with non-d^0 cations, successfully stabilizing the voltage profiles. Since the replacement was done with a mixture of four different cations, high lattice distortions are present, activating more 1-TM channels and making more Li^+ accessible. This work opens new possibilities for the design of high-energy-density Li-excess cathode materials with a unique combination of the rate capability of ordered materials, and the compositional flexibility of DRX.

5. Experimental Section

Synthesis: The materials were synthesized using a solid-state route. Li_2CO_3 (Alfa Aesar, 99%), $Cr_3(OH)_2(CH_3CO_2)_7$ (Sigma Aldrich, 23–25% Cr), TiO_2 (anatase, Alfa Aesar, 99.9%), Al_2O_3 (Sigma Aldrich, nanopowder), MnO_2 (Sigma Aldrich, 99%), Fe_2O_3 (Sigma Aldrich, nanopowder), and MoO_3 (Alfa Aesar, 99.5%) were used as precursors. The precursors were weighed in a stoichiometric ratio, except for Li_2CO_3, which was added in 10% excess to compensate for Li loss during the synthesis, and mixed together in ethanol using a Retsch PM 200 planetary ball mill at 250 rpm for 12 h. After drying, the mixture was pelletized and sintered under an Ar atmosphere at 850 °C for 12 h, followed by furnace cooling. The pellets were transferred to an Ar-filled glovebox and manually ground in a mortar.

Electrochemistry: Cathode film preparation and coin cell assembly were conducted in an Ar-filled glovebox. In a typical process, the active material was hand mixed in a mortar with Super C65 carbon black (Timcal) for 30 min. Then, polytetrafluoroethylene (PTFE, DuPont), was added to the mixture and rolled into a thin film. The weight ratio of active material to carbon to binder was 7:2:1. The electrodes were cut with a 5/16-inch punch. The active material loading was controlled to be between 3 and 4 mg cm^{-2}. The R2032 coin cells were assembled with a metallic Li anode (FMC), glass microfiber separator (Whatman), and 80 µl of commercial electrolyte 1 M $LiPF_6$ in ethylene carbonate (EC) and dimethyl carbonate (DMC) in 1:1 volume ratio (Sigma Aldrich). Before every test, the cells rested for at least 6 h. The electrochemical tests were performed using an Arbin battery cycler at 25 °C. For the galvanostatic intermittent titration technique (GITT) measurements, the assembled cells were charged/discharged in the voltage range of 1.5–4.8 V for two cycles at a current of 20 mA g^{-1} for 30 min

© 2025 The Author(s). Advanced Energy Materials published by Wiley-VCH GmbH

16146840, 0, Downloaded from https://advanced.onlinelibrary.wiley.com/doi/10.1002/aenm.202502157, Wiley Online Library on [16/06/2025]. See the Terms and Conditions (https://onlinelibrary.wiley.com/terms-and-conditions) on Wiley Online Library for rules of use; OA articles are governed by the applicable Creative Commons License

(10 mAh g^{-1} step) with the following 6 h relaxation step. For the ex situ characterizations, the cells were (dis)charged to a selected state at a current of 20 mA g^{-1}, kept at the constant voltage for 6 h, and then disassembled in an Ar-filled glovebox and washed with diethyl carbonate (DEC) solvent. In the case of ex situ XRD measurements, electrodes containing polyvinylidene fluoride (PVDF) instead of PTFE were used, because a reflection from PTFE overlaps with the peak from the layered R-3m phase at ca. 18.5°.

Characterization: The crystal structure of the studied partially disordered materials was investigated by the X-ray diffraction (XRD) method, using a Panalytical Empyrean diffractometer in θ-θ Bragg-Brentano geometry with Cu Kα radiation, equipped with a PIXcel 3D detector. For the as-synthesized powders, the patterns were measured at room temperature in the 10–110° range with a resolution of 0.013° for ca. 51 min, while for the electrodes (ex situ samples), the range was 10–90° and the measurement lasted 60 min. The patterns were qualitatively analyzed using Panalytical HighScore software. For Rietveld refinements, GSAS-II software[76] was utilized, with the details of the fitting process provided in Note S2 (Supporting Information). The microstructure and particle size of the obtained powders were studied by scanning electron microscopy (SEM) using Thermo Fisher Scientific Phenom XL with an accelerating voltage of 15 kV. The experiments were conducted in backscattered electron mode. For the structural characterization using transmission electron microscopy (TEM), the samples were drop-casted onto carbon-coated copper grids. TEM, selected area electron diffraction (SAED), and high angle annular dark field (HAADF) scanning TEM coupled with energy dispersive X-ray spectroscopy (STEM+EDS) measurements were carried out using Thermo-Fisher Scientific Titan Themis XFEG 200 kV S/TEM, equipped with a probe Cs-corrector.

Hard X-Ray Absorption Spectroscopy: Hard X-ray absorption spectroscopy (hXAS) studies were conducted at 7-BM Quick X-ray Absorption and Scattering beamline, Brookhaven National Laboratory, with Si(111) monochromator in transmission mode. K-edges for Cr, Ti, Mn, Fe, and Mo were probed. Reference foils for a given element were measured simultaneously for energy calibration. All the samples were sealed in a polyimide foil inside an Ar-filled glovebox. The collected spectra were processed, including normalization and calibration, using Athena software.[77] To obtain the extended X-ray absorption fine structure (EXAFS) spectra, the background was subtracted using the built-in Autobk algorithm with R_{bkg} set to 0.95. The spectra were converted from energy space to k-space, and then Fourier transformed to R-space. The presented spectra were k^2-weighted. The phase correction was not applied, so the real distances in R-space should be ca. 0.3-0.4 Å longer.[22]

Soft X-Ray Spectroscopies—Resonant Inelastic X-Ray Spectroscopy (RIXS): The O K-edge, Cr, Ti, Mn, Fe L_3-edge RIXS spectra were collected by iRIXS endstation at beamline 8.0.1 in Advanced Light Source, Lawrence Berkeley National Laboratory. The high-resolution detector was used for the O K-edge and Ti L_3-edge scans, and the high-throughput detector was used for the Fe and Mn scans. Both detectors were used for Cr L_3-edge scans, high-resolution for RIXS cut, and high-throughput for the mapping of RIXS (mRIXS). A homemade transfer kit was used to transfer the samples from an Ar-filled glovebox to the measurement chamber to avoid air exposure. The O-K RIXS spectra were continuously scanned through the region of interest with the excitation energy step size of 0.2 eV and dwelling time of 90 s. Ti L_3-edge RIXS spectra were collected at four excitation energies of 457.2, 458, 458.8, and 460 eV with a dwelling time of 300 s to check possible dd-transitions arising from non-4+ Ti species. Cr L_3-edge RIXS cuts were collected at four excitation energies of 574.5, 576.7, 578.7, and 580.9 eV with a dwelling time of 300 s to check dd-transition arising from non-6+ Cr species. Fe, Mn, and Cr L_3-edge RIXS spectra were continuously scanned through the region of interest with the excitation energy step size of 0.2 eV and dwelling time of 60 s. To minimize beam damage, the specimen was repeatedly moved up and down by 0.5 mm during measurement, and it was confirmed that the spectrum was well averaged due to the long dwelling time. The collected spectra were fabricated to 2D RIXS maps as functions of emission and excitation energies. Further processing, including normalization, cosmic ray removal, etc., had been conducted for the 2D maps as in the previous work.[78]

Soft X-Ray Spectroscopies—Soft X-Ray Absorption Spectroscopy (sXAS): Cr, Mn, and Fe L_3-edge soft X-ray absorption spectra by total electron yield (TEY) mode, which represents the surface properties (> 10 Å from the surface of materials), were simultaneously collected during the RIXS spectra collection. Ti L_3-edge sXAS TEY spectra were separately collected with a dwelling time of 2 s per point and were summed after 3 repetitive scans.

Soft X-Ray Spectroscopies—RIXS Map-(inverse) Partial Fluorescence Yield (mRIXS-(i)PFY) Method for sXAS Spectra Collection of Cr, Mn, and Fe L_3-Edges: To avoid the distortion from O K-edge emission to Cr, Mn, and Fe L_3-edge fluorescence spectra, mRIXS-(i)PFY mode was employed.[57] In mRIXS spectra, which were obtained at the given excitation energies of TMs L_3-edge, a specific energy range of fluorescence could be selectively extracted, and it is named partial fluorescence yield here (PFY). The Mn and Fe L_3-edge sXAS spectra without distortion from the O K-edge emission line are collected by the mRIXS-PFY. On the other hand, O K-edge emission lines were selectively extracted from the Cr L_3-edge mRIXS spectra and plotted as a function of excitation energy. The inversion of the plot corresponds to the sXAS spectra of pure bulk without distortion and was named inverse partial fluorescence yield (iPFY) here, as done in the previous report.[78]

Supporting Information

Supporting Information is available from the Wiley Online Library or from the author.

Acknowledgements

This work was supported by the Assistant Secretary for Energy Efficiency and Renewable Energy, Vehicle Technologies Office, of the U.S. Department of Energy under Contract No. DE-AC02-05CH11231, under the Advanced Battery Materials Research (BMR) Program. The Advanced Light Source, where soft X-ray spectroscopies were measured, is supported by the Director, Office of Science, Office of Basic Energy Sciences, of the U.S. Department of Energy under contract no. DE-AC02-05CH11231. M.M. and K.Ś. were supported by the National Science Centre, Poland, (NCN) on the basis of the decision number UMO-2019/35/O/ST5/01560. M.M. was supported by the Polish National Agency for Academic Exchange (NAWA Preludium Bis 1) on the basis of the decision PPN/STA/2021/1/00022/DEC/1. M.M. was supported by the Foundation for Polish Science (FNP).

Conflict of Interest

The authors declare no conflict of interest.

Data Availability Statement

The data that support the findings of this study are available from the corresponding author upon reasonable request.

Keywords

cathode materials, cation disordered rocksalt, cation migration, lithium-ion batteries, partially disordered layered structure

Received: April 16, 2025
Revised: May 21, 2025
Published online:

---

[1] E. A. Olivetti, G. Ceder, G. G. Gaustad, X. Fu, *Joule* **2017**, *1*, 229.

© 2025 The Author(s). Advanced Energy Materials published by Wiley-VCH GmbH

16146840, 0, Downloaded from https://advanced.onlinelibrary.wiley.com/doi/10.1002/aenm.202502157, Wiley Online Library on [16/06/2025]. See the Terms and Conditions (https://onlinelibrary.wiley.com/terms-and-conditions) on Wiley Online Library for rules of use; OA articles are governed by the applicable Creative Commons License

[2] Z. P. Cano, D. Banham, S. Ye, A. Hintennach, J. Lu, M. Fowler, Z. Chen, *Nat. Energy* **2018**, *3*, 279.
[3] J. U. Choi, N. Voronina, Y. K. Sun, S. T. Myung, *Adv. Energy Mater.* **2020**, *10*, 202002027.
[4] Z. Yang, H. Huang, F. Lin, *Adv. Energy Mater.* **2022**, *12*, 202200383.
[5] P. K. Nayak, E. M. Erickson, F. Schipper, T. R. Penki, N. Munichandraiah, P. Adelhelm, H. Sclar, F. Amalraj, B. Markovsky, D. Aurbach, *Adv. Energy Mater.* **2018**, *8*, 1702397.
[6] R. J. Clément, Z. Lun, G. Ceder, *Energy Environ. Sci.* **2020**, *13*, 345.
[7] J. Lee, A. Urban, X. Li, D. Su, G. Hautier, G. Ceder, *Science* **2014**, *343*, 519.
[8] D. Chen, J. Ahn, G. Chen, *ACS Energy Lett.* **2021**, *6*, 1358.
[9] J. Lee, D. A. Kitchaev, D. H. Kwon, C. W. Lee, J. K. Papp, Y. S. Liu, Z. Lun, R. J. Clément, T. Shi, B. D. McCloskey, J. Guo, M. Balasubramanian, G. Ceder, *Nature* **2018**, *556*, 185.
[10] A. Urban, J. Lee, G. Ceder, *Adv. Energy Mater.* **2014**, *4*, 1400478.
[11] Z. Jadidi, T. Chen, L. Barroso-Luque, G. Ceder, *Chem. Mater.* **2023**, *35*, 9225.
[12] Z. Jadidi, T. Chen, P. Xiao, A. Urban, G. Ceder, *J. Mater. Chem. A.* **2020**, *8*, 19965.
[13] Y. Sun, S. Jiao, J. Wang, Y. Zhang, J. Liu, X. Wang, L. Kang, X. Yu, H. Li, L. Chen, X. Huang, *J. Am. Chem. Soc.* **2023**, *145*, 11717.
[14] H. Li, R. Fong, M. Woo, H. Ahmed, D. H. Seo, R. Malik, J. Lee, *Joule* **2022**, *6*, 53.
[15] R. Qi, I. Konuma, Y. Kaneda, M. Kondo, N. Yabuuchi, *Chem. Mater.* **2022**, *34*, 1946.
[16] G. H. Lee, J. Lim, J. Shin, L. J. Hardwick, W. Yang, *Front. Chem.* **2023**, *11*, 1098460.
[17] Y. Zhang, A. Hu, J. Liu, Z. Xu, L. Mu, S. Sainio, D. Nordlund, L. Li, C. J. Sun, X. Xiao, Y. Liu, F. Lin, *Adv. Funct. Mater.* **2022**, *32*, 202110502.
[18] M. Nakajima, N. Yabuuchi, *Chem. Mater.* **2017**, *29*, 6927.
[19] L. Huang, P. Zhong, Y. Ha, Z. Cai, Y. W. Byeon, T. Y. Huang, Y. Sun, F. Xie, H. M. Hau, H. Kim, M. Balasubramanian, B. D. McCloskey, W. Yang, G. Ceder, *Adv. Energy Mater.* **2023**, *13*, 2202345.
[20] E. Lee, D. H. Lee, S. Bessette, S. W. Park, N. Brodusch, G. Lazaris, H. Kim, R. Malik, R. Gauvin, D. H. Seo, J. Lee, *Energy Environ. Sci.* **2024**, *17*, 3753.
[21] Z. Cai, B. Ouyang, H. M. Hau, T. Chen, R. Giovine, K. P. Koirala, L. Li, H. Ji, Y. Ha, Y. Sun, J. Huang, Y. Chen, V. Wu, W. Yang, C. Wang, R. J. Clément, Z. Lun, G. Ceder, *Nat. Energy* **2023**, *9*, 27.
[22] J. Huang, P. Zhong, Y. Ha, D. H. Kwon, M. J. Crafton, Y. Tian, M. Balasubramanian, B. D. McCloskey, W. Yang, G. Ceder, *Nat. Energy* **2021**, *6*, 706.
[23] I. Konuma, D. Goonetilleke, N. Sharma, T. Miyuki, S. Hiroi, K. Ohara, Y. Yamakawa, Y. Morino, H. B. Rajendra, T. Ishigaki, N. Yabuuchi, *Nat. Mater.* **2023**, *22*, 225.
[24] S. Hoshino, A. M. Glushenkov, S. Ichikawa, T. Ozaki, T. Inamasu, N. Yabuuchi, *ACS Energy Lett.* **2017**, *2*, 733.
[25] H. Ji, A. Urban, D. A. Kitchaev, D. H. Kwon, N. Artrith, C. Ophus, W. Huang, Z. Cai, T. Shi, J. C. Kim, H. Kim, G. Ceder, *Nat. Commun.* **2019**, *10*, 592.
[26] L. Li, B. Ouyang, Z. Lun, H. Huo, D. Chen, Y. Yue, C. Ophus, W. Tong, G. Chen, G. Ceder, C. Wang, *Nat. Commun.* **2023**, *14*, 7448.
[27] Z. Lun, B. Ouyang, D. H. Kwon, Y. Ha, E. E. Foley, T. Y. Huang, Z. Cai, H. Kim, M. Balasubramanian, Y. Sun, J. Huang, Y. Tian, H. Kim, B. D. McCloskey, W. Yang, R. J. Clément, H. Ji, G. Ceder, *Nat. Mater.* **2021**, *20*, 214.
[28] A. G. Squires, D. O. Scanlon, *J. Mater. Chem. A* **2023**, *11*, 13765.
[29] S. Zhou, Y. Sun, T. Gao, J. Liao, S. Zhao, G. Cao, *Angew. Chem.* **2023**, *135*, 202311930.
[30] Z. Cai, Y. Q. Zhang, Z. Lun, B. Ouyang, L. C. Gallington, Y. Sun, H. M. Hau, Y. Chen, M. C. Scott, G. Ceder, *Adv. Energy Mater.* **2022**, *12*, 202103923.
[31] Y. Wang, S. Huang, B. Raji-Adefila, A. Outka, J. H. Wang, D. Chen, *J. Am. Chem. Soc.* **2022**, *144*, 19838.
[32] J. Ahn, R. Giovine, V. C. Wu, K. P. Koirala, C. Wang, R. J. Clément, G. Chen, *Adv. Energy Mater.* **2023**, *13*, 2300221.
[33] T. Holstun, T. P. Mishra, L. Huang, H. M. Hau, S. Anand, X. Yang, C. Ophus, K. Bustillo, L. Ma, S. Ehrlich, G. Ceder, *Adv. Energy Mater.* **2024**, *37*, 2412871.
[34] X. Mi, H. Li, X. Huang, *J. Power Sources* **2007**, *174*, 867.
[35] X. Mi, H. Li, X. Huang, *Electrochem. Solid-State Lett.* **2006**, *9*, A324.
[36] L. Zhang, H. Noguchi, *J. Electrochem. Soc.* **2003**, *150*, A601.
[37] Y. N. Ko, S. H. Choi, Y. C. Kang, S. B. Park, *J. Power Sources* **2013**, *244*, 336.
[38] M. D. Radin, S. Hy, M. Sina, C. Fang, H. Liu, J. Vinckeviciute, M. Zhang, M. S. Whittingham, Y. S. Meng, A. Van der Ven, *Adv. Energy Mater.* **2017**, *7*, 1602888.
[39] W. Zuo, M. Luo, X. Liu, J. Wu, H. Liu, J. Li, M. Winter, R. Fu, W. Yang, Y. Yang, *Energy Environ. Sci.* **2020**, *13*, 4450.
[40] N. Li, M. Sun, W. H. Kan, Z. Zhuo, S. Hwang, S. E. Renfrew, M. Avdeev, A. Huq, B. D. McCloskey, D. Su, W. Yang, W. Tong, *Nat. Commun.* **2021**, *12*, E4.
[41] A. Urban, A. Abdellahi, S. Dacek, N. Artrith, G. Ceder, *Phys. Rev. Lett.* **2017**, *119*, 176402.
[42] M. Hamaguchi, H. Momida, A. Kitajou, S. Okada, T. Oguchi, *Electrochim. Acta* **2020**, *354*, 136630.
[43] O. F. Dippo, K. S. Vecchio, *Scr. Mater.* **2021**, *201*, 113974.
[44] Y. Zeng, B. Ouyang, J. Liu, Y. W. Byeon, Z. Cai, L. J. Miara, Y. Wang, G. Ceder, *Science* **2022**, *378*, 1320.
[45] J. Zheng, W. H. Kan, A. Manthiram, *ACS Appl. Mater. Interfaces* **2015**, *7*, 6926.
[46] K. Zhou, Q. Xie, B. Li, A. Manthiram, *Energy Storage Mater.* **2021**, *34*, 229.
[47] H. Zhang, K. Karki, Y. Huang, M. S. Whittingham, E. A. Stach, G. Zhou, *J. Phys. Chem. C* **2017**, *121*, 1421.
[48] H. Feng, Y. Leng, T. Chen, Y. Sun, C. Hai, Y. Zhou, *J. Alloys Compd.* **2023**, *960*, 170676.
[49] K. Ku, J. Han, L. Li, J. Gim, J. Park, B. Shi, Y. Liang, A. Stark, C. Wang, J. R. Croy, M. M. Thackeray, J. Libera, E. Lee, *J. Electrochem. Soc.* **2023**, *170*, 050511.
[50] E. Lee, J. Blauwkamp, F. C. Castro, J. Wu, V. P. Dravid, P. Yan, C. Wang, S. Kim, C. Wolverton, R. Benedek, F. Dogan, J. S. Park, J. R. Croy, M. M. Thackeray, *ACS Appl. Mater. Interfaces* **2016**, *8*, 27720.
[51] H. Zhang, F. Omenya, M. S. Whittingham, C. Wang, G. Zhou, *ACS Energy Lett.* **2017**, *2*, 2598.
[52] S. Choi, A. Manthiram, *J. Electrochem. Soc.* **2002**, *149*, A1157.
[53] E. Rossen, J. N. Reimers, J. R. Dahn, *Solid State Ionics* **1993**, *62*, 53.
[54] J. Lee, C. Wang, R. Malik, Y. Dong, Y. Huang, D. H. Seo, J. Li, *Adv. Energy Mater.* **2021**, *11*, 202100204.
[55] J. Huang, B. Ouyang, Y. Zhang, L. Yin, D. H. Kwon, Z. Cai, Z. Lun, G. Zeng, M. Balasubramanian, G. Ceder, *Nat. Mater.* **2023**, *22*, 353.
[56] M. Balasubramanian, J. McBreen, I. J. Davidson, P. S. Whitfield, I. Kargina, *J. Electrochem. Soc.* **2002**, *149*, A176.
[57] A. J. Achkar, T. Z. Regier, E. J. Monkman, K. M. Shen, D. G. Hawthorn, *Sci. Rep.* **2011**, *1*, 182.
[58] N. M. Trease, I. D. Seymour, M. D. Radin, H. Liu, H. Liu, S. Hy, N. Chernova, P. Parikh, A. Devaraj, K. M. Wiaderek, P. J. Chupas, K. W. Chapman, M. S. Whittingham, Y. S. Meng, A. Van Der Van, C. P. Grey, *Chem. Mater.* **2016**, *28*, 8170.
[59] J. Wu, Z. Zhuo, X. Rong, K. Dai, Z. Lebens-Higgins, S. Sallis, F. Pan, L. F. J. Piper, G. Liu, Y. de Chuang, Z. Hussain, Q. Li, R. Zeng, Z. xun Shen, W. Yang, *Sci. Adv.* **2020**, *6*, aaw3871.
[60] J. Wu, Y. Yang, W. Yang, *Dalton Trans.* **2020**, *49*, 13519.

© 2025 The Author(s). Advanced Energy Materials published by Wiley-VCH GmbH

16146840, 0, Downloaded from https://advanced.onlinelibrary.wiley.com/doi/10.1002/aenm.202502157, Wiley Online Library on [16/06/2025]. See the Terms and Conditions (https://onlinelibrary.wiley.com/terms-and-conditions) on Wiley Online Library for rules of use; OA articles are governed by the applicable Creative Commons License

[61] K. Zhang, Y. Chen, Y. Zhu, Q. Zheng, Y. Tang, D. Yu, Q. Liu, H. Luo, J. Yin, L. Zeng, W. Jiao, N. Liu, Q. Wang, L. Zheng, J. Zhang, Y. Wang, B. Zhang, Y. Yan, H. Huang, C. H. Shen, Y. Qiao, S. G. Sun, *Angew. Chem., Int. Ed.* **2025**, *64*, 202419909.

[62] B. Ammundsen, J. Paulsen, I. Davidson, R.-S. Liu, C.-H. Shen, J.-M. Chen, L.-Y. Jang, J.-F. Lee, *J. Electrochem. Soc.* **2002**, *149*, A431.

[63] X. Zhao, Y. Tian, Z. Lun, Z. Cai, T. Chen, B. Ouyang, G. Ceder, *Joule* **2022**, *6*, 1654.

[64] X. Zhao, G. Ceder, *Joule* **2022**, *6*, 2683.

[65] Y. Lyu, N. Zhao, E. Hu, R. Xiao, X. Yu, L. Gu, X. Q. Yang, H. Li, *Chem. Mater.* **2015**, *27*, 5238.

[66] N. Yabuuchi, K. Yamamoto, K. Yoshii, I. Nakai, T. Nishizawa, A. Omaru, T. Toyooka, S. Komaba, *J. Electrochem. Soc.* **2013**, *160*, A39.

[67] E. J. Wu, P. D. Tepesch, G. Ceder, *Philos. Mag. B Phys. Condens. Matter; Stat. Mech. Electron. Opt. Magn. Prop.* **1998**, *77*, 1039.

[68] Y. Lyu, L. Ben, Y. Sun, D. Tang, K. Xu, L. Gu, R. Xiao, H. Li, L. Chen, X. Huang, *J. Power Sources* **2015**, *273*, 1218.

[69] X. Zheng, Z. Xu, S. Li, Y. Zhang, J. Zhang, C. Kuai, L. Tao, M. M. Rahman, Y. Zhang, S. J. Lee, C. J. Sun, L. Li, W. Hu, D. Nordlund, J. Liu, Y. Liu, F. Lin, *Acta Mater.* **2021**, *212*, 116935.

[70] S. Ren, R. Chen, E. Maawad, O. Dolotko, A. A. Guda, V. Shapovalov, D. Wang, H. Hahn, M. Fichtner, *Adv. Sci.* **2015**, *2*, 1500128.

[71] W. Wang, J. Meng, X. Yue, Q. Wang, X. Wang, Y. Zhou, X. Yang, Z. Shadike, Z. Fu, *Chem. Commun.* **2018**, *54*, 13809.

[72] S. Kim, X. Ma, S. P. Ong, G. Ceder, *Phys. Chem. Chem. Phys.* **2012**, *14*, 15571.

[73] N. Takeda, I. Ikeuchi, R. Natsui, K. Nakura, N. Yabuuchi, *ACS Appl. Energy Mater.* **2019**, *2*, 1629.

[74] W. Liu, J. Li, W. Li, H. Xu, C. Zhang, X. Qiu, *Nat. Commun.* **2020**, *11*, 3629.

[75] Y. Tesfamhret, R. Younesi, E. J. Berg, *J. Electrochem. Soc.* **2022**, *169*, 010530.

[76] B. H. Toby, R. B. Von Dreele, *J. Appl. Crystallogr.* **2013**, *46*, 544.

[77] B. Ravel, M. Newville, *J. Synchrotron Radiat.* **2005**, *12*, 537.

[78] G. H. Lee, J. Wu, D. Kim, K. Cho, M. Cho, W. Yang, Y. M. Kang, *Angew. Chem., Int. Ed.* **2020**, *59*, 8681.

© 2025 The Author(s). Advanced Energy Materials published by Wiley-VCH GmbH

16146840, 0, Downloaded from https://advanced.onlinelibrary.wiley.com/doi/10.1002/aenm.202502157, Wiley Online Library on [16/06/2025]. See the Terms and Conditions (https://onlinelibrary.wiley.com/terms-and-conditions) on Wiley Online Library for rules of use; OA articles are governed by the applicable Creative Commons License